Article

Low Energy Implantation into Transition Metal Dichalcogenide Monolayers to Form Janus Structures
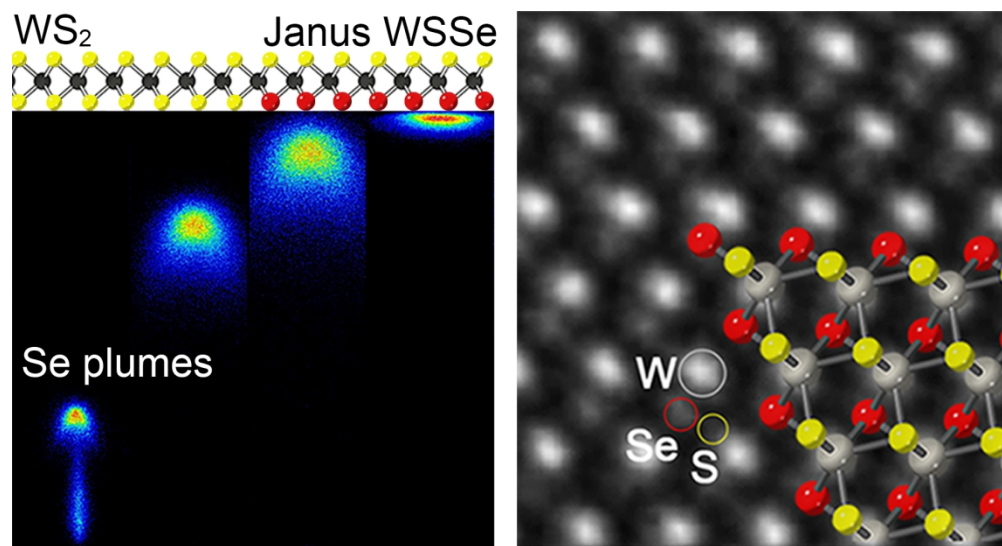
Yu-Chuan Lin, Chenze Liu, Yiling Yu, Eva Zarkadoula, Mina Yoon, Alexander A. Puretzky, Liangbo Liang, Xiangru Kong, Yiyi Gu, Alex Strasser, Harry M. Meyer, Matthias Lorenz, Matthew F. Chisholm, Ilia N. Ivanov, Christopher M. Rouleau, Gerd Duscher, Kai Xiao, and David B. Geohegan

Just Accepted

The kinetic energies of Se clusters in pulsed laser deposition plasma plumes are tuned < 10 eV/atom to controllably and easily convert monolayer WS_2 crystals into Janus WSSe monolayers by implantation at < 300°C.

Low Energy Implantation into Transition Metal Dichalcogenide Monolayers to Form Janus Structures

Yu-Chuan Lin,[a] Chenze Liu,[b] Yiling Yu,[a] Eva Zarkadoula,[c] Mina Yoon,[a] Alexander A. Puretzky,[a] Liangbo Liang,[a] Xiangru Kong,[a] Yiyi Gu,[b,d] Alex Strasser,[a,e] Harry M. Meyer III,[c] Matthias Lorenz,[a] Matthew F. Chisholm,[a] Ilia N. Ivanov,[a] Christopher M. Rouleau,[a] Gerd Duscher,[b] Kai Xiao,[a] and David B. Geohegan[a,*]

a. Center for Nanophase Materials Sciences, Oak Ridge National Laboratory, Oak Ridge, Tennessee 37831, United States
b. Department of Materials Science and Engineering, University of Tennessee, Knoxville, Tennessee 37996, United States
c. Materials Science and Technology Division, Oak Ridge National Laboratory, Oak Ridge, Tennessee 37831, United States
d. Key Laboratory of Photochemical Conversion and Optoelectronic Materials, Technical Institute of Physics and Chemistry, Chinese Academy of Sciences, Beijing 100190, China.
e. Department of Chemical Engineering, Texas A&M University, College Station, Texas, 77840, United States

*Email: geohegandb@ornl.gov

1
2
3
4
5
6
7
8
9
10
11
12
13
14
15
16
17
18
19
20
21
22
23
24
25
26
27
28
29
30
31
32
33
34
35
36
37
38
39
40
41
42
43
44
45
46
47
48
49
50
51
52
53
54
55
56
57
58
59
60

Abstract

Atomically-thin two-dimensional (2D) materials face significant energy barriers for synthesis and processing into functional metastable phases such as Janus structures. Here, the controllable implantation of hyperthermal species from pulsed laser deposition (PLD) plasmas is introduced as a top-down method to compositionally engineer 2D monolayers. The kinetic energies of Se clusters impinging on suspended monolayer WS_2 crystals were controlled in the <10 eV/atom range with *in situ* plasma diagnostics to determine the thresholds for selective top layer replacement of sulfur by selenium for the formation of high quality WSSe Janus monolayers at low (300 °C) temperatures, and bottom layer replacement for complete conversion to WSe_2. Atomic-resolution electron microscopy and spectroscopy in tilted geometry confirm the WSSe Janus monolayer. Molecular dynamics simulations reveal that Se clusters implant to form disordered metastable alloy regions, which then recrystallize to form highly ordered structures, demonstrating low-energy implantation by PLD for the synthesis of 2D Janus layers and alloys of variable composition.

Keywords

Janus monolayer, 2D materials, transition metal dichalcogenide, implantation, synthesis and processing, conversion, pulsed laser deposition

Compositional engineering can greatly expand the functionality of atomically-thin two-dimensional (2D) materials. For instance, the incorporation of foreign transition metal or chalcogen atoms in the MX_2 transition metal dichalcogenide (TMD, M = Mo, W, and X = S, Se, Te) semiconductors[1,2] to form ternary or quaternary alloys can enhance optoelectronic properties by tuning the bandgap, suppressing defects, or controlling the crystal phase.[3–9] The thermodynamic stability and miscibility of the constituent atoms determines the stability of random 2D alloys.[3,10]

Janus monolayer TMDs are intriguing compositionally-engineered 2D materials in which different chalcogens occupy the top and bottom of a monolayer (ML).[11–13] The broken symmetry and permanent dipole moment inherent in Janus monolayers offer enhanced functionality, such as piezoresponse,[12,14] catalytic behavior,[13] and charge separation.[11] While bottom-up, physical and chemical vapor deposition methods can readily form 2D TMD mixed alloys,[5,8] Janus monolayers have not yet been successfully synthesized by these techniques. Instead, top-down processing of TMD ML have been employed. For example, $MoSe_2$ ML can be sulfurized at high temperatures (750-850 °C) to form Janus MoSSe, taking advantage of the higher cohesive energy of MoS_2 *vs* $MoSe_2$.[15] However, to form Janus MoSSe by selenizing MoS_2 ML, hydrogen plasmas were employed to first sputter away the upper sulfur layer before introduction of selenium vapor at high temperatures.[12] Unfortunately, both methods induced significant levels of defects, evident by weak photoluminescence and crack formation.

This generation of a vacancy in the sublattice has been regarded as the barrier for atomic substitution in an existing 2D crystal. Density functional theory (DFT) calculations and molecular dynamics (MD) simulations indicate that most of the constituent chalcogen atoms in 2D TMDs have relatively low displacement energies (T_d) ranging from 5 to 7 eV, while $T_d > 20$ eV for the transition metal atoms.[16,17] The displacement of chalcogen atoms has been achieved under exposure to an 80-100 keV electron beam.[16] High-energy ions (e.g., 500 eV Ar^+)[18] are typically utilized to attempt chalcogen

sputtering, however, it may also lead to unnecessary defect formation. As a result, moderate kinetic energy (KE) in the 10-100 eV range are being explored.[19–22] A different approach is to directly implant atoms of choice into 2D materials with ~10 eV energies suitable for displacement and substitution of the original species.[22] Ideally, such sources could provide a wide spectrum of elements and tunable KE < 10 eV.

Pulsed laser deposition (PLD) is a versatile method to explore the synthesis of advanced thin films by depositing materials generated by the laser ablation of solid targets. In laser-ablation plasmas used for PLD the KE of species can exceed 100 eV in vacuum, allowing the synthesis of metastable phases (e.g., amorphous diamond by laser ablation of graphite).[23] PLD of sulfur in vacuum was shown to controllably replace Se atoms in monolayer $MoSe_2$ crystals at 700 °C to digitally tune the composition of $MoS_{2x}Se_{2(1-x)}$ alloys, eventually resulting in total conversion to MoS_2 with successive pulses.[4] A great advantage of PLD is the ability to moderate the KE of species arriving at the substrate using background gas collisions.[23–25]

In this work, we explore precise tailoring of the hyperthermal nature of pulsed laser ablation plasmas to implant Se species with KE < 10 eV/atom into WS_2 ML. We first determine the thresholds for soft landing, for selenization limited to the top-most S layer, and for selenization of the bottom S layer. Then we demonstrate that by controlling the KE, selective and complete selenization of the top layer of suspended or supported WS_2 ML can be achieved to form high-quality Janus WSSe ML at low (300 °C) temperatures in an implantation and recrystallization process described by molecular dynamics and density functional theory simulations.

Results and Discussion

Hyperthermal Se species with KE < 42 eV/atom were naturally generated by laser vaporization of a solid Se target in vacuum and were directed toward WS$_2$ ML crystals on TEM grids or substrates as shown in Fig. 1a. The plasma plume propagation was measured by a combination of *in situ* intensified-CCD array (ICCD) photography of its visible luminescence (Fig. 1b) and ion probe current waveforms measured at different positions (Fig. 1c). By adding 5-50 mTorr of argon, the plasma plume was decelerated controllably to tune the maximum KE of species arriving at the substrate from 42 eV/atom in
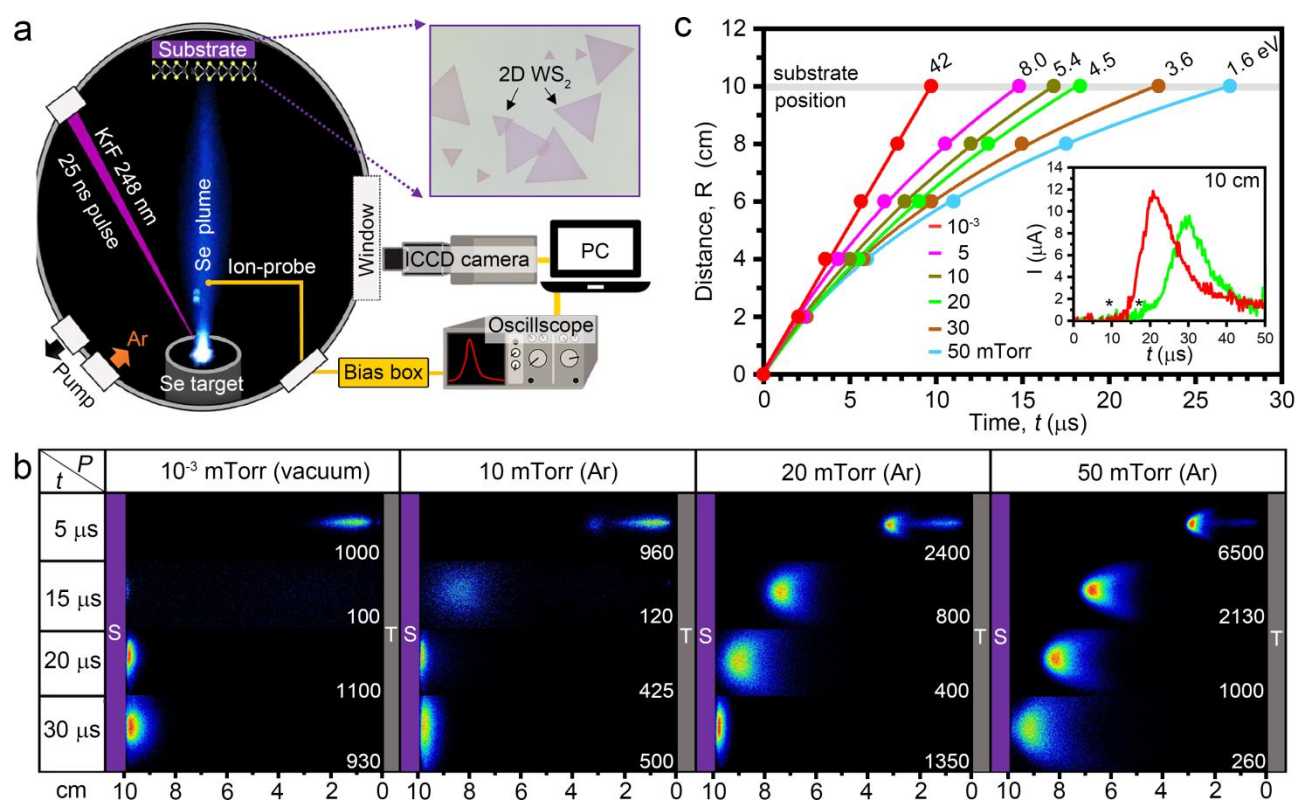
Fig. 1. *in situ* diagnostics of Se plasma plumes (a) Experimental setup for Se plasma plume generation and impingement on CVD-grown WS$_2$ ML within a vacuum chamber equipped with an ICCD camera and a translatable probe for ion-flux measurement. Excimer laser pulses (248 nm, 25 ns, 1 Hz, 1 Jcm^{-2}) irradiate a 1-inch Se target at 30º generating a highly forward-directed plasma plume. (b) False color, gated-ICCD images of the Se plasma's visible luminescence reveal the plume's propagation dynamics through vacuum and 10, 20, and 50 mTorr argon background gas pressures at the indicated delay times following the laser pulse. (Gate width is 10% of each delay time, maximum intensity is shown for comparison.) (c) R-*t* plots of the leading edge of the plasma (from ion probe currents, see * in inset) track the propagation and deceleration in different background Ar pressures. The propagation for each pressure is fit by the a $= -\alpha v^2$ drag model, where R $= \alpha^{-1}\ln(1 + \alpha v_o t)$ and v $= v_o(1 + \alpha v_o t)^{-1}$, from which the maximum Se kinetic energy/atom at the d = 10 cm substrate position could be adjusted (shown, also see SI Note 1 and Fig. S1).

vacuum, to < 1 eV/atom at 100 mTorr. The plume deceleration followed a standard a = - αv^2 drag model (Figs. 1c, S1),[26,27] however the small deceleration coefficient compared to typical atomic and molecular plasmas,[25] along with its highly forward-directed angular distribution and weak luminescence, implied that its main constituents were clusters.[26,27]

Laser desorption/ionization time-of-flight mass spectrometry (Fig. S2) revealed that the plume is composed principally of clusters ranging from Se_2 to Se_9, consistent with prior measurements for laser-vaporized Se.[28,29] The weakly-ionized plasma travels at maximum velocities of ~ 1 cm/µs in vacuum (Fig. 1b) and is only weakly luminescent until arrival at the substrate, where collisions within the boundary layer result in comparatively brighter emission. Similarly, confinement of the plasma by the Ar gas during propagation results in significantly enhanced emission intensity as shown in Figs. 1c, S3. This broadband emission (Figs. S3, S4) displays vibronic modes characteristic of Se_2^*. Laser-induced fluorescence confirmed that Se_2 clusters are prevalent in the as-vaporized distribution. As the background gas collisions slow the plume, collision-induced dissociation of the larger clusters[30–32] likely result in the ejection of Se_2 clusters which have the highest dissociation energy (3.52 eV) of all the Se_n clusters.[30,31,33] As a result selenium dimers are likely the predominant species arriving at the substrate as the pressures are raised in these experiments. Only trace evidence for atomic Se* emission was observed in the near-substrate collisional zone (Fig. S4).

WS_2 MLs were exposed to Se plasma plumes with different maximum KEs. The substrates were held at 250°C to desorb excess Se within 1 ms after each pulse arrived, as measured by time-resolved optical reflectivity. After deposition, Raman and photoluminescence (PL) micro-spectroscopies were used to gauge the extent of conversion of the WS_2 crystals for equal numbers of Se pulses using different KEs. As shown in Fig. 2a, for 800 Se pulses at pressures ≥ 40 mTorr, corresponding to KE ≤ 3 eV/atom, the
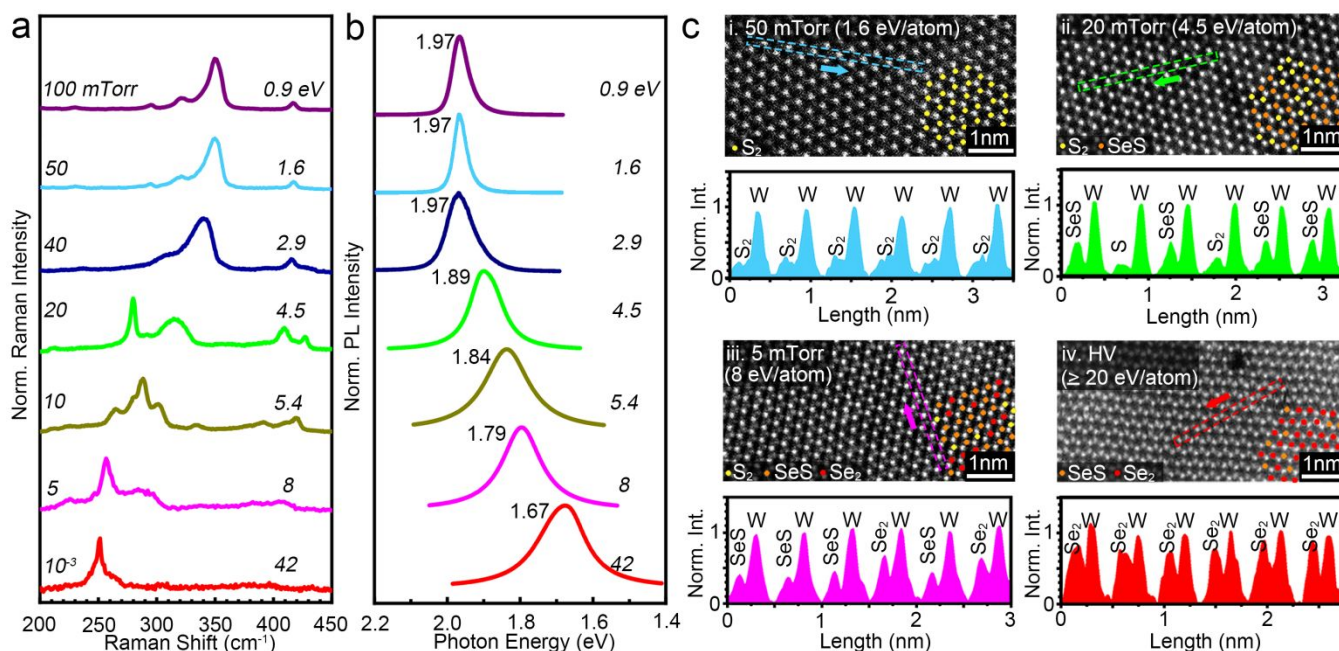
Fig. 2. Characterizations of WS$_{2(1-x)}$Se$_{2x}$ ML converted from WS$_2$ by Se plasma plumes (a) Raman spectra of WS$_2$ ML on SiO$_2$/Si substrates exposed by 800 Se plasma plume pulses in different background Ar pressures at 250 °C. Spectra indicate an increasing fraction of Se incorporation in WS$_{2(1-x)}$Se$_{2x}$ with decreasing Ar pressure. (b) Corresponding PL spectra and peak energy positions of the irradiated WS$_2$ MLs measured in (a). (c) HAADF Z-contrast STEM images of WS$_2$ ML suspended on TEM grids and irradiated by Se plasma plumes arriving through Ar pressures with maximum KEs: i) 50 mTorr (1.6 eV/atom, 800 pulses), ii) 20 mTorr (4.5 eV/atom, 800 pulses), iii) 5 mTorr (8 eV/atom, 600 pulses), and iv) 10^{-6} Torr (≥ 20 eV/atom, 600 pulses). Chalcogen columns containing S-S, Se-S, and Se-Se pairs in the images are labeled with yellow, orange, and red balls based on their Z-contrast intensity (based on Z$^{1.9}$ scaling) with respect to W, revealing: At 50 mTorr no Se incorporation is detected; At 20 mTorr Se-S pairs are evident; At 5 mTorr Se-Se also appear, in addition to Se-S; In high vacuum (HV), most S-S pairs have been replaced with Se-Se and Se-S. The line profiles below each panel compare the relative Z-contrast intensity between W and dichalcogenide sites.

characteristic (2LA(M)+E')[34] Raman peak at 350 cm^{-1} of WS$_2$ ML was barely affected, indicating little or no selenization. Corresponding PL peak positions were unaffected from unexposed WS$_2$ ML until 40mTorr, where spectral broadening became noticeable. When the pressure was lowered to 20 mTorr, corresponding to < 4.5 eV/atom, two predominant Raman peaks measured at 278 cm^{-1} and 320 cm^{-1} resemble out-of-plane and in-plane vibrations of a Janus WSSe ML predicted at 277 cm^{-1} and 322 cm^{-1} (and See SI Note 3-4),[35] indicating that the upper S layer was largely replaced with Se. With further increase in KE, the Raman and PL spectra continue to transform until the Raman peak at 251 cm^{-1} and PL peak at 1.67 eV of WSe$_2$ ML were obtained, indicating full conversion of WS$_2$ to WSe$_2$. However, as shown in Fig. S5, the weak PL intensity for KE > 4.5 eV/atom necessitated 600 °C substrate temperatures

to recover comparable signal intensity, indicating that higher kinetic energy species induce lattice damage that can be effectively healed with moderate temperatures.

To understand atomistic effects of the KE-dependent selenization process, WS_2 ML crystals were suspended on TEM grids, exposed to Se plume pulses under the same conditions, and then examined using high angle annular dark field (HAADF) Z-contrast scanning transmission electron microscopy (Z-STEM). The samples exhibit 3 regimes, summarized in Fig. 2c: (i) For low KE < 3 eV/atom, no perceptible Se incorporation or lattice damage was observed. (ii) At 4.5 eV/atom, significant replacement of S by Se in the lattice was confirmed by image contrast line profiles which reveal columns containing S-Se pairs but not Se-Se pairs. The fraction of S-Se pairs approach 100% with increasing numbers of shots, suggesting that just the atoms in the top S layer might be selenized to form Janus MLs. (iii) For higher KE, ($\geq$ 5.4 eV/atom) columns containing Se-Se pairs appear in higher concentration in addition to Se-S pairs, suggesting penetration of Se to the lower layer of S atoms.

DFT calculations were performed to understand the migration barrier for a Se adatom to penetrate through an undamaged WS_2 ML. As shown in Fig. S6, an 8.8 eV/Se barrier can be expected depending upon the chosen path.

In order to understand the dependence of cluster size and kinetic energy on implantation depth and kinetic mechanisms, MD simulations of Se_2 and Se_9 clusters impacting with suspended WS_2 were performed spanning our experimental 1.6-42 eV/atom KE range (Figs. 3a, 3b and S7, S8). Details of the MD simulation code, interatomic potentials employed, and a comparison of predicted defect energetics with those from first principles calculations can be found in Methods and in Note 2 of the Supporting Information. At 1.6 eV/atom the Se_2 cluster soft-lands on the surface, consistent with studies estimating the limit for soft landing as one half the binding energy of a cluster.[36] At this energy, Se_9 clusters similarly
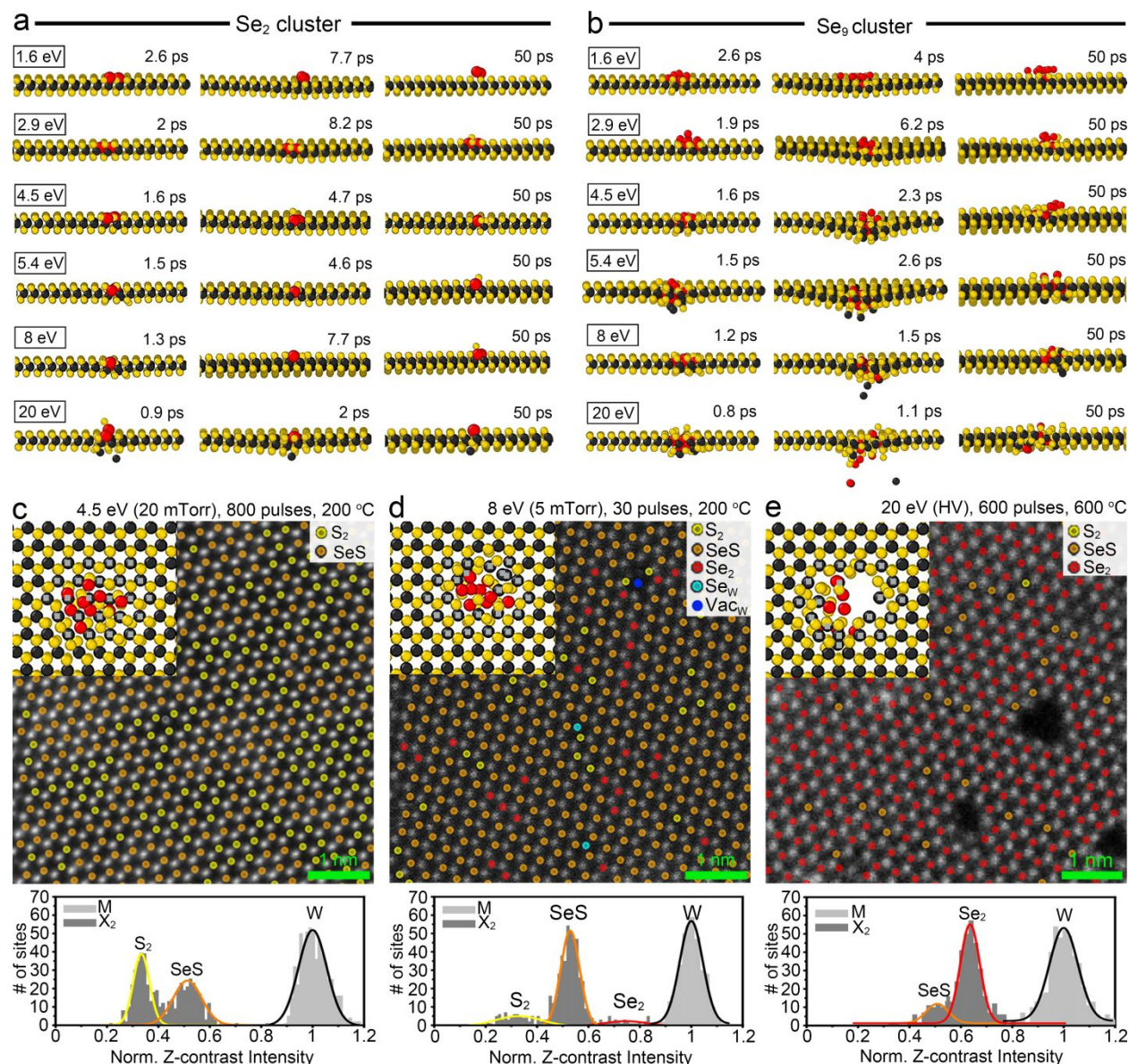
Fig. 3. MD simulations of Se$_2$ and Se$_9$ clusters impacting on suspended WS$_2$ ML and comparative HAADF STEM images. (a) Se$_2$: With 1.6 eV/atom, MD simulations predict that a Se$_2$ cluster softly lands on WS$_2$ ML without damaging it, with 4.5-8 eV/atom the Se$_2$ implants to displace the top S atoms in WS$_2$ ML, and with 20 eV/atom is capable of penetrating WS$_2$ ML to displace and begin to sputter the W atoms. (b) Se$_9$: With 1.6 eV/atom, a Se$_9$ cluster also softly lands. With 4.5 eV/atom, Se implants the top S layer. With 5.4 eV and 8 eV/atom, Se implants through the entire WS$_2$ ML displacing, and then beginning to sputter the W atoms. For $\geq$ 20 eV/atom, significant damage to WS$_2$ ML occurs *via* sputtering of W and S atoms. (c-e) Top views of Z-contrast STEM image of WS$_2$ ML irradiated by Se plasma plumes with 4.5, 8, and 20 eV/atom. Insets show top-view MD simulation snapshots of Se$_9$ implantations at the same KEs, captured 50 ps after impact where the W atoms around the impact zone were highlighted with cyan squares to better see their positions. (c) After 800 plume pulses at 200 °C with 4.5 eV/atom, despite significant selenization no damage to the W lattice positions was detectable. (d) After 30 Se plume pulses with 8 eV/atom, both antisite defects (Se$_W$), or missing W due to sputtering (Vac$_W$) are evident, consistent with the MD simulations. In addition, selenization of the ML includes Se-Se columns that were absent in 4.5 eV/atom case appear (marked by red circles), consistent with penetration of Se to the bottom layer. (e) For higher KE ($\geq$ 20 eV/atom) Se clusters, larger pores result, resembling the predicted MD image.

land, but deform. Neither cluster displaces the top S atoms, consistent with our $\geq$ 50 mTorr observations. At 2.9 eV/atom only the Se_9 cluster displaces a S atom. This threshold coincides with the theoretical substitutional barrier for replacing a S atom by Se predicted by Li *et al.* (2.81 eV/atom).[9] With 4.5 eV/atom, Se_2 and Se_9 clusters implant effectively into the ML, yet displace only the top layer of S atoms. The implanted Se atoms do not penetrate beyond the W layer, nor do they displace the W atoms as shown in the inset to Fig. 3c. HAADF-STEM images (as shown in Fig. 3c) confirm that after 800 pulses at 200 °C, about half of the S-S pairs have been converted to Se-S pairs but no W-related defects are observed. For higher KE, the heavier clusters more efficiently implant into the bottom layer of S atoms, and also displace W atoms. As shown in Fig. 3b, this occurs at $\geq$ 5.4 eV/atom for Se_9, however for Se_2 this occurs for $\geq$ 20 eV/atom. Fig. 3d shows that after 30 pulses for 8.0 eV/atom at 200°C, S-S pairs are being efficiently converted to Se-S but W-vacancies and anti-site defects are also being created, consistent with the MD simulations.

At higher energies, such as shown in the inset of Fig. 3e for 20 eV, the Se_9 cluster collisions can sputter W and S atoms to cause pores and the irreparable loss of W. Substitution of both top and bottom S layers becomes very efficient with increasing KE as the lighter clusters increasingly penetrate through the entire monolayer. Significantly, selenization in 20 mTorr Ar with $\leq$ 4.5 eV/atom preserves strong PL at low temperatures of 250°C (Fig. S5). However, photoluminescence is quenched for crystals that were selenized at 250°C by Se species with maximum KE $\geq$ 8 eV/atom. This loss of PL for KE $\geq$ 8 eV/atom agrees with the significant structural rearrangement predicted by the MD simulations for these higher energies. However, increasing the deposition temperature to 600 °C allows the recovery of strong PL for even the highest KE of 42 eV/atom (Fig. S5). As Fig. 3e shows for this case, despite the irreparable loss of W atoms at pores caused by the larger cluster, the rest of the W atoms reconstruct during the 600 pulse

(2 min) deposition process at 600 °C to form a well-ordered $WS_{2(1-x)}Se_{2x}$ crystal that is nearly fully selenized.

Following the energetic implantation of Se atoms the time scales for W atom migration, as well as the time for elimination of the excess S and Se atoms to reconstruct the crystal, are not yet determined experimentally. However, MD simulations (performed at 1100 K to accelerate the dynamics, Fig. S9) lend some insight into how Se replaces S in the lattice. Following the impact of a Se cluster, the implanted Se atoms displace S atoms to form what appears to be a disordered, Se-rich, amorphous alloy in a localized region. Fig. S10 shows an experimental image of excess Se that is implanted with KE ≤ 8 eV/atom and still preserved at RT after cooling from deposition at 200 °C. This image appears very similar to the simulation shown in the inset of Fig. 3d. As these disordered zones recrystallize, Se atoms occupy some of the prior S sites while excess S and Se diffuse away, presumably driven by entropic mixing. As the simulations show, physisorbed surface S atoms tend to migrate and then evaporate selectively (although both S and Se evaporate) to leave a selenized crystal after each Se pulse.

The experimental data, theory, and simulations all indicate that controlling selenium KE ≤ 4.5 eV/atom should selenize only the top layer of S atoms in WS_2 without causing W atom displacement, enabling the formation of a Janus WSSe ML. Therefore, WS_2 MLs suspended on TEM grids or supported on SiO_2/Si substrates were held at 300 °C and exposed to 2000 Se plume pulses (at 5 Hz) in 20 mTorr Ar gas. The samples directly converted on TEM grids were first imaged by Z-contrast STEM as shown in Fig. 4a, 4b to identify the chalcogen compositions by their Z-contrast. As shown in Fig. 4c, a histogram of image intensities scaled (by $Z^{1.9}$) to the intensity of the W atom peak, reveals that all of the chalcogen columns can be assigned to Se-S pairs (and not S, Se, S-S, or Se-Se), consistent with Janus ML formation.

To understand whether the substituted Se atoms were all situated on one side of the ML, the TEM grid was tilted by 15° around both x- and y-axes and re-imaged to get a perspective view, as shown in
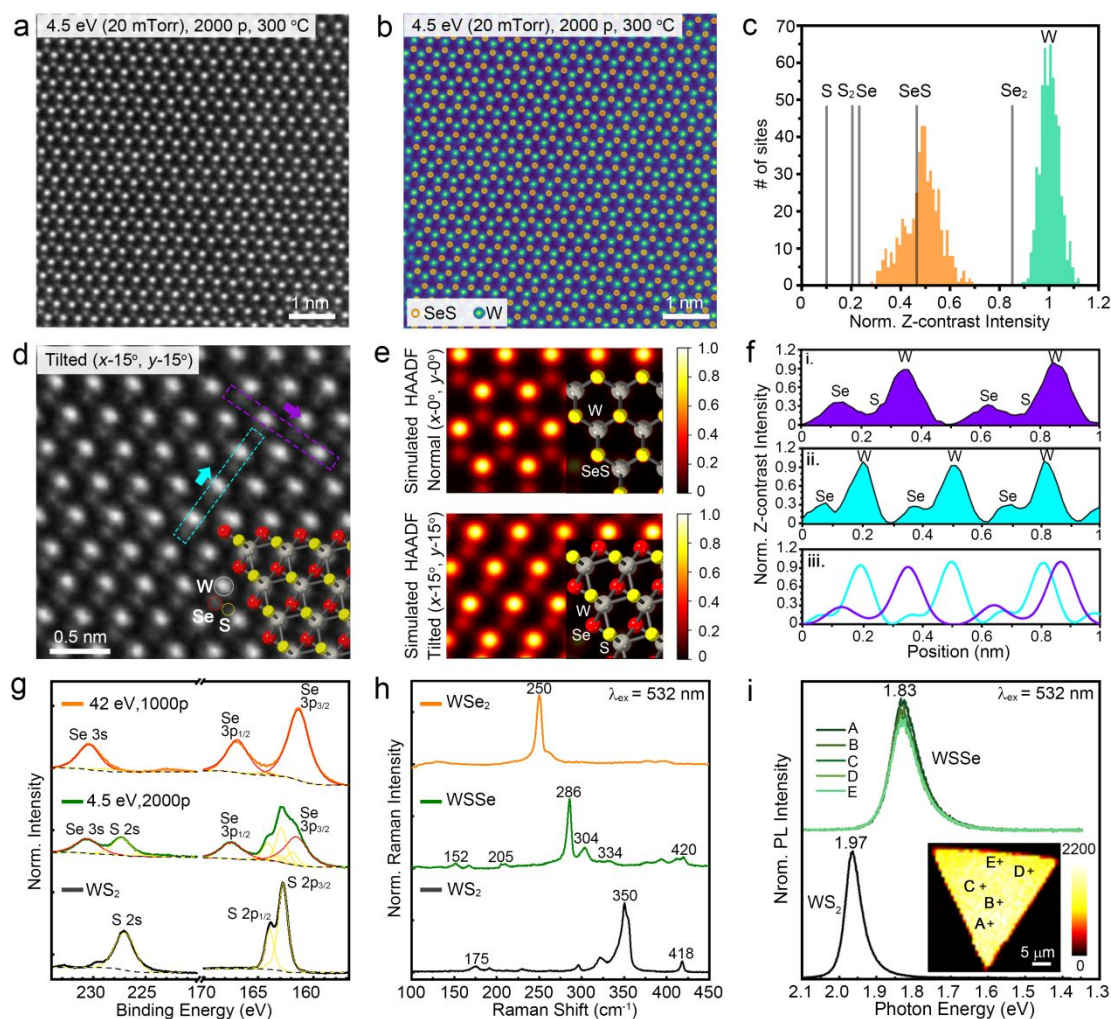
Fig. 4. Characterization of Janus WSSe ML formed by Se implantation in WS$_2$. (a) Normal view HAADF Z-contrast STEM image of WS$_2$ ML irradiated by 2000 Se plume pulses at < 4.5 eV/atom shows a uniform contrast between metal sites and chalcogen columns. (b) Same image as in (a) where Se-S sites and W sites are colored orange and green, respectively, based on intensity analysis compared to W sites assuming Z$^{1.9}$ scattering intensity. (c) Histogram shows the numbers of W and Se-S pairs found in (b), indicating full conversion of S-S into Se-S. The reference lines mark the expected intensities for S, S-S, Se, and Se-Se in the X$_2$ column relative to the center of the W intensity distribution, based on Z$^{1.9}$. (d) A tilted HAADF Z-STEM image (x-15°, y-15°) permits visualization of both top and bottom atoms of a Janus WSSe ML (as schematically shown in the bottom-right corner where Se(red) and S(gold) become displaced). (e) Simulated Z-contrast STEM image intensities and models (insets) for the Janus WSSe ML in normal (top) and tilted (bottom) views agree well with the experimental STEM images. (f) i) and ii) intensity line profiles from (d) match well with iii) the simulated intensity from an idealized Janus structure. (g) XPS analysis (400 μm spot size) deconvoluting the *s*- and *p*- orbital contributions for CVD-grown WS$_2$ ML, for WSSe ML formed from 2000 Se pulses at 4.5 eV/atom at 600 °C yielding Se:S of 1.08:1 , and for fully converted WSe$_2$ ML from 1000 Se pulses of < 42 eV/atom Se at 600 °C. (h) Raman characteristic peaks of Janus WSSe ML are located midway between the peaks of WS$_2$ ML and converted WSe$_2$ ML. (i) Photoluminescence spectra of unirradiated WS$_2$ ML before selenization, and Janus WSeS ML after selenization. Five different spots from the PL map shown in inset show little variation in their PL intensity and spectral position across a converted domain. (Raman and PL spectra were excited by a 532 nm laser. Each spot in the PL map was measured with 50 μW power with 2s accumulation.)

Fig4d. A comparison of the HAADF image with the overlaid ball-and-stick model shows that the Se atoms

are all located on one side of the monolayer and the Se-S pairs are oriented in the same direction across

the image, which corresponds to a Janus structure. For comparison, simulated HAADF images from a

Janus ML in both normal and tilted views are shown in Fig. 4e. The images and simulated linescan

intensities in Fig. 4f agree well with the experimental images. The experimental tilted images were also

compared with simulated tilted views of pure WS_2 and WSe_2 ML (Fig. S11) to confirm the presence and

uniformity of the Janus ML. In addition, other tilt angles were explored to confirm that the projected image

changed accordingly. For example, a comparison of experimental and simulated tilted HAADF-STEM

images for a rotation about x = +15º of 2D WSSe are shown in Fig. S12. The projections of S and Se are

displaced as expected, however not as far as the relatively large distance in the HAADF image of Fig. 4

with a tilt angle of x = +15º and y = +15º, which permitted a more straightforward intensity analysis.

X-ray photoelectron spectroscopy (XPS) was performed on CVD-grown WS_2 continuous ML

films on sapphire exposed to Se plume pulses in either 20 mTorr Ar or 10^{-6} Torr at 600 ºC, respectively.

As shown in Fig. 4g, the chalcogen binding energy spectra for 42 eV/atom Se exposure is well-fit by the

Se-*3s*/-*3p* orbitals consistent with complete conversion of WS_2 to WSe_2. The sample exposed at < 4.5

eV/atom can be deconvoluted using a mixture of the Se-*3s*/-*3p* orbital lineshapes with the characteristic

S-*2s*/-*2p* lineshapes from pristine WS_2 where the integrated intensity from Se and S orbitals agree within

10% (Se:S is 1.08), consistent with full conversion to Janus WSSe.

Raman and PL micro-spectroscopy measurements, summarized in Figs. S13-S15**,** were performed

on single-domain WS_2 ML grown on SiO_2/Si and exposed to selenium plumes with KE ≤ 4.5 eV/atom. In

addition, we performed first principles modeling to calculate the predicted Raman spectra for Janus TMD

MLs. The characteristic Raman spectrum of WS_2 is transformed after low-energy selenization to reveal

vibrational modes that agree within 2 cm^{-1} of our predicted A$_1$ (284 cm^{-1}, 422 cm^{-1}) and E (204 cm^{-1}, 335 cm^{-1}) for Janus WSSe ML (Fig. S13), and are consistent with other predictions.[35] Optical micrograph and scanning electron microscopic images indicate the surface of converted Janus ML is continuous and crack-free (Fig. S16). Finally, the measured PL peak at 1.83 eV for the selenized WS$_2$ MLs, matches the theoretically predicted value for the direct optical bandgap of a Janus WSSe ML.[35,37] As shown in Figs. 4i, S15e, the strong and uniform characteristic PL of the Janus WSSe ML across the 30-micron single-crystal domain of supported WS$_2$ that was selenized by this process. Thus, the XPS, Raman and PL spectroscopy measurements indicate that high-quality Janus WSSe MLs observed locally in HAADF-STEM imaging extend over large crystalline domains.

To test whether Janus monolayers of other crystals can be similarly formed by low-energy implantation, we explored the selenization of single-domain MoS$_2$ ML crystals grown by CVD on SiO$_2$/Si. Although an independent theoretical study was not carried out to determine the predicted defect energetics for this system, by utilizing the same optimal conditions experimentally determined for conversion of ML WS$_2$ to WSSe Janus monolayers we found that supported MoS$_2$ can be also be easily transformed to Janus MoSSe. As shown in Fig. S13b, the original vibrational modes of MoS$_2$ ML at E' (384 cm^{-1}) and A$_1$' (404 cm^{-1}) were transformed to the characteristic A$_1$ (290 cm^{-1}) and E (355 cm^{-1}) of a Janus MoSSe ML, consistent (within 3-5 cm^{-1}) with our theoretically predicted spectra in Fig. S13d . The measured PL peak at 1.76 eV shown in Fig. S13f is also consistent with our theoretically predicted value.

Conclusions

In summary, moderating the natural hyperthermal kinetic energy of species inherent within pulsed laser deposition plasmas to < 10 eV has revealed the thresholds for selenization of suspended WS_2 monolayer crystals, summarized in Fig. 5, including a ~3-5 eV/atom window for the low-temperature (< 300 °C) formation of high-quality Janus WSSe ML. Our preliminary results (Table 1, Fig. S13) indicate that other Janus structures such as MoSSe can also be synthesized by this approach. The combined experimental and theoretical results indicate that this non-equilibrium synthesis process permits materials of interest to be controllably implanted to different depths within atomically thin layers. The key to the process is the implantation of extra atoms to form high energy defect structures that are Se-rich and disordered. First principles calculations (Fig. S17) estimate that 4.5 eV/atom Se_9 impacts can impart ~ 9
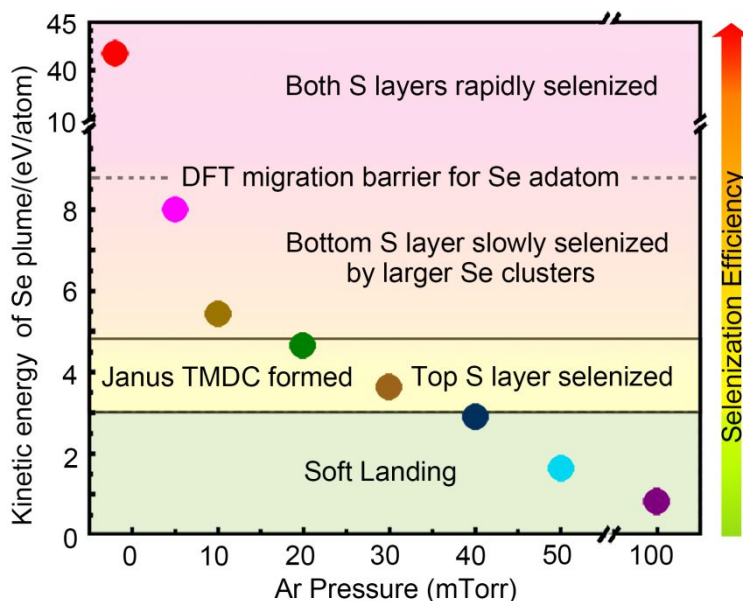
Fig. 5. Summary diagram of KE regimes for selenization of WS_2 ML by implantation using Se PLD. Points indicate maximum KEs measured from Se plume leading edge arriving at suspended WS_2 MLs placed at 10 cm as shown in Fig. 1 for different background Ar gas pressures. For ≥ 40 mTorr selenium species soft-land inducing no selenization or damage, then desorb for > 200 °C. Selenization of only the top S layer of WS_2 ML suitable for Janus WSSe formation occurs between 20-40 mTorr for Se plume KEs between 3-4.5 eV/atom. At low pressures (≤ 20 mTorr) and plume KEs above 5.4 eV/atom, selenization of the bottom S layer by larger Se clusters increases and becomes rapidly once pressures decrease towards vacuum.

eV/nm^2 localized energy in such structures, to overcome the natural energy barrier for selenization from WS_2. These isolated metastable zones within the 2D crystal can subsequently recrystallize at moderate temperatures to expel the excess S (and Se). This implantation process overcomes a significant fraction of the barrier ≤ 8.8 eV/Se for a single Se adatom to diffuse to the bottom layer. For low KE (3-5 eV/atom) for Janus layer formation, the damage is localized in the top chalcogen layer of the monolayer, and recrystallization into a Janus ML requires < 300 °C.

However, Se implantation to the lower chalcogen layer can be achieved experimentally by Se species with 5-8 eV/atom KE, which MD simulations indicate is due to the larger (Se_9) cluster impacts that are well known in cluster deposition to cause greater damage.[38] These impacts are also sufficient to displace W atoms. At even higher energies, such as 40 eV/atom, rapid selenization of both layers occurs despite the irreparable loss of W atoms caused by these larger Se clusters. In both cases, moderate 600 °C substrate temperatures allow the crystal to self-repair, returning displaced W atoms to their lattice sites and reorganizing pores.

Through repeated Se implantation and recrystallization, the WS_2 crystal can be fully converted into either Janus WSSe or WSe_2 MLs, with the extent of alloying controlled by the number of Se dose pulses. These results provide valuable insights to guide the bottom-up PLD synthesis of 2D materials and to develop hyperthermal implantation as a top-down method to explore the synthesis of metastable 2D Janus layers and alloys of variable composition.

Methods

Pulsed Laser Deposition of Se and *in situ* Diagnostics. A pulsed KrF (248 nm, 25ns FWHM, 1-5 Hz repetition rate) laser was used for the ablation of the targets in vacuum and argon background gas. A 1 in.-diameter selenium pellet (Plasmaterials, Inc., 99.99% purity) was used as the ablation target. Using a projection beamline, an aperture was imaged from an aperture onto the target to produce a 1.25 mm x 4.5 mm rectangular spot. Typically, 57 mJ of energy was used, providing 1.0 J/cm^2 per laser pulse at the target surface. WS$_2$ monolayer crystals grown by CVD on SiO$_2$/Si substrates were mounted on a 1 in. diameter heater (HeatWave Laboratories, Inc.) placed d = 10 cm away from the Se target in a cylindrical stainless-steel chamber (50 cm inner diameter, 36 cm tall). The heater temperature was controlled to ± 2 °C *via* a PID controller, and ramp-rates were typically 30 °C/min. The gas pressure was controlled with a mass flow controller (Ar 99.995%, 10 standard cubic centimeters per minute (sccm)) and a downstream throttle valve.

Imaging of the visible luminescence of the plasma plume (or laser-induced fluorescence (LIF)) was performed with a gated-ICCD camera (Princeton Instruments ST-130) with variable gate width (5 ns minimum). The camera was triggered by a digital delay generator (SRS DG 545) which was triggered by a fast photodiode at the exit of the KrF laser. The camera lens (Nikon, f4.5) was positioned 46 cm away from the center of the plume, outside the chamber and through a 2 in x 8 in fused silica (Suprasil) window. In low-light situations, the exposure time was typically set to 10% of the delay time. Ion probe current waveforms (-40 V floating bias supplied by a battery and 1 μF decoupling capacitor, detector area ~ 1 mm^2) were recorded by a digitizing oscilloscope (LeCroy WaveJet 354T) using 1 or 5 kΩ input impedance.

Simultaneous spectroscopy also could be performed using a second gated, intensified CCD-array detector (PI-MAX 3, Princeton Instruments) that was coupled to a spectrometer (Spectra Pro 2300i, Acton, f = 0.3 m, 150, 600, and 1200 grooves/mm gratings). Light from the plume was collected using a 2-inch, f = 0.5 m lens outside the chamber, through a 2 in x 8 in fused silica (Suprasil) window located opposite the former window. Different collection positions could be chosen by sliding the spectrometer and lenses on a translation table. For the laser induced fluorescence (LIF) experiments, the third harmonic of a Nd:YAG laser (355 nm, 8 ns pulse width, 1 Hz repetition rate) was triggered (at a time delay selected on the delay generator relative to the KrF-laser ablation pulse) to irradiate the plume species at different distances from the target, and the spectroscopy CCD-detector could be gated to collect light during this pulse, or afterward, using the delay generator.

Transient deposition and desorption of Se species were detected on tailored SiO_2/Si substrates using a specularly-reflected HeNe laser beam which was passed through the windows of the chamber, through a 633nm filter, and onto a fast photodiode (Thorlabs SM1PD1A).[39] The transient decrease in reflectivity was recorded on a digitizing oscilloscope (LeCroy WaveJet 354T) to estimate the arrival and residence times at different temperatures and pressures.

Synthesis of WS_2 and MoS_2 monolayers.   CVD synthesis of WS_2 monolayers was performed using sulfur powder (Sigma-Aldrich) that was placed 20 cm upstream from the center heat zone where WO_3 (10 mg, 99.99%, Sigma-Aldrich) powder mixed with 3% of KCl powder (Sigma-Aldrich), by mass, was placed. SiO_2/Si substrates also were placed in the center of the 2 in. tube furnace, face down above the powders. A typical growth run was performed at 820°C-850 °C for 5 min under a flow of Ar gas at 60 sccm and ambient pressure. CVD MoS_2 monolayers, specifically, were grown using a mixture of MoO_3 (5 mg) and S powders at 750 °C for 4-6 min under a flow of Ar gas at 70 sccm and ambient pressure.

Sample preparation and HAADF STEM experiments for alloys monolayers on TEM grids. A thin layer of poly(methyl methacrylate) (PMMA) was deposited onto a substrate with WS_2 monolayers in a spin-coater (500 rpm for 10 s and 3000 rpm for 50 s) and then left in a fume hood overnight to evaporate the solvent. The PMMA-coated monolayers on SiO_2/Si substrate were placed in a Petri dish filled with KOH solution (30 wt%, 90 °C) to dissolve the substrate, leaving a PMMA/WS_2 membrane. The membrane was transferred onto a SiN_x grid (Ted Pella) with 2.5 μm holes, and then washed in acetone and isopropyl alcohol to remove the PMMA. Prior to electron microscopy experiments, the samples were directly implanted and selenized on TEM grids in the PLD chamber. The TEM grids were baked at 160 °C overnight in vacuum before STEM measurements to remove residual hydrocarbons.

The HAADF Z-contrast STEM characterization was conducted in a Nion Ultra STEM 200 microscope with sub-angstrom resolution operated at 100 kV. The STEM-ADF image simulation for the normal and tilted views of an ideal Janus WSSe ML was performed using the QSTEM simulation package.[40] WSSe Janus ML model consists $10\times10\times1$ unit cells. The probe array was 400×400 pixels with a resolution of 0.05 Å. The high voltage was 100 kV, convergence angle was 30 mrad, the brightness was 5×10^8 $Acm^{-2}sr^{-1}$, temperature was 300 K, and the detector geometry was 70 to 200 mrad. For normal view image simulation, the sample tilt angle was 0°, while for tilted view image simulation, the sample tilt was set to x = +15° and y= +15°.

Analysis of HAADF STEM images.

Stacks of images were registered first registered rigidly and then with a Diffeomorphic Demon Non-Rigid Registration as provided by the simpleITK package.[41] These registered images of a stack were summed along the time axi s resulting in images with high signal noise ratio. We also used single images again with high spatial resolution and high contrast. The atom positions were determined with a two-step process in which first, the most common blob detection based on the Lapalacian of Gaussian (implemented in the scipy package) was performed. Any atom detection algorithm will lead to the same result as the blob detector for such high contrast images. Then a Gaussian was fitted to each blob to obtain sub-pixel precision in atom position. An affine distorted lattice was fitted to the W atom sites and the rough position of the chalcogenide site was determined by a shift of the W-atoms lattice. The chalcogenide atom positions were further refined by determination of the position centered in the middle of the three nearest neighbor W atoms, to observe local distortions. The atom positions were used to sum over the same-sized circular area around an atom position separately for the two different sublattices. The intensity-histograms of the two sublattices can then be plotted independently. This approach makes it possible to detect vacancy and low intensity atom sites, even though no atomic column is visible in the image.

Spectroscopic material characterizations. Raman and photoluminescence spectra were acquired in a Renishaw Raman spectroscopy system equipped with a 532 nm excitation laser focused on the samples through a 100x, 0.8 NA objective. Raman and PL spectra were gathered using 3000 groves/mm and 300 groves/mm grating, respectively. The excitation laser power was ≤ 100 µW to avoid damaging the samples. Collection was performed at room temperature and in the ambient conditions.

X-ray photoelectron spectroscopy. X-ray photoelectron spectroscopy (XPS) was performed using a Thermo Scientific (Waltham, MA, USA) Model K-Alpha XPS instrument. The instrument utilizes monochromated, micro-focusing, Al Kα X-rays (1486.6 eV). Analyses of the samples were all conducted with a 400 µm X-ray spot size for maximum signal and to obtain an average surface composition over the largest possible area on continuous and highly-uniform CVD WS_2 monolayer films grown on c-sapphire (2D Semiconductors, Inc.). The instrument has a hemispherical electron energy analyzer equipped with a 128 multi-channel detector system. Base pressure in the analysis chamber is typically 2×10^{-9} mbar or lower. Substrates with the WS_2 samples were attached to the XPS sample holder with metal clips. Survey spectra (pass energy = 200 eV) were acquired for qualitative and quantitative analysis, and high-resolution core level spectra (pass energy = 50 eV) were acquired for detailed chemical state analysis. All spectra were acquired with the aid of a charge neutralization flood gun to maintain stable analysis conditions. It uses a combination of low energy electrons and Ar ions for optimum charge compensation, and the typical

pressures in the analysis chamber during operation was ~2 x 10^{-7} mbar. Data were collected and processed using the Thermo Scientific Avantage XPS software package (v.5.96). Peak fitting was performed using mixed Gaussian/Lorentzian peak shapes and a Shirley/Smart type background. The fitted doublet peaks originating from the S 2p and Se 3p orbitals for the layer selenized in 20 mTorr (4.5 eV) Ar are located at (162.8; 164) eV and (161.5; 167.3) eV, respectively. It is worth noting that the peaks originating from W 4f orbital in WS^2 and converted WSSe layer are nearly identical.

Matrix-Assisted Laser Desorption Ionization (MALDI). To understand the range of cluster sizes emitted from UV nanosecond laser-vaporized Se targets in vacuum, a commercial Bruker MALDI-TOF Autoflex LRF instrument was employed. A 1-micron thick film of Se was laser deposited onto a gold substrate without any matrix and irradiated at 1 kHz using a Nd-YAG laser. The spectrum was formed with 300 individual laser shots at separate locations on the substrate.

Molecular dynamics simulations for Se cluster impact. LAMMPS[42] was used for the MD simulations, and the WS_2 monolayers were 18 nm × 16 nm in size. Periodic boundary conditions were used along the x and y dimensions of the MD box, and shrink-wrapped boundary conditions along the z direction. The interatomic potentials utilized by Mobaraki *et al.*[43] for WS_2 were used for all interactions, and joined with the Ziegler-Biersack-Littmark (ZBL) potentials[44] to describe short range interactions between the atoms. The systems of the monolayers and the clusters were relaxed for 500 ps (0.5 fs timestep) prior to the ion implantation, and at 100 K to eliminate thermal vibration effects. The Se clusters used to investigate the implantation consisted of 2 and 9 Se-atom clusters (Se_2 and Se_9), and their energies were varied from 1.6 eV/atom up to 42 eV/atom. The implantation was normal to the sample surface to simulate the experimental plume interaction with the substrate. The irradiation simulations were performed for 50 ps in the microcanonical (NVE) ensemble, using scaling of the energy at the MD box boundaries to emulate the larger sample in experiments.

For simulations of the post-implantation annealing (of the Se_9 cluster that had been implanted into WS_2 with 8 eV/atom) the system was further relaxed for 50 ps. Subsequently, to simulate long-term annealing effects, the system was raised to high (1000 K or 1100 K) temperatures and run for 2 ns (1 fs timesteps). Note that the atoms belonging to the lower layer of S were fixed during these thermal annealing simulations, and all the MD results were visualized using Ovito.[45]

A comparison between the defect energetics predicted from first principles calculations and the effective interatomic potentials utilized in the MD simulations is presented in the Supporting Information.

First principles calculations for the energetics of selenization. Our first-principles calculations are based on density functional theory (DFT) as implemented in the Vienna *ab initio* simulation package (VASP)[46] with a projector-augmented method. A local density approximation[47] was used for the exchange-correlation functional with the energy cutoff of the plane-wave basis set at 500 eV, and with a k-mesh having a k-spacing of $\sim 2\pi \times 0.05 \text{Å}^{-1}$ for the self-consistent total energy calculation. The Se-implanted structural configurations resulting from the classical MD simulation were fully relaxed without k-point sampling in order to simulate the defective region created by a single shot implantation. In all the calculations, a 20 Å vacuum layer was used and all atoms were fully relaxed until the residual forces on each atom were less than 0.01 eV/Å.

First principles calculations for phonon and Raman scattering. Plane-wave DFT calculations also were carried out using the VASP package. The projector augmented-wave (PAW) pseudopotentials were used for electron-ion interactions, and the local density approximation (LDA) was adopted to describe exchange-correlation interactions. LDA has been shown to produce a satisfactory description of both the electronic and vibrational properties of TMDs such as MoS_2 and WSe_2.[48,49] For monolayer TMDs and the Janus systems, including MoS_2, $MoSe_2$, WS_2, WSe_2, MoSSe, and WSSe, the energy cutoff was set at 350 eV and the k-point sampling was chosen as $24 \times 24 \times 1$. They were simulated by a periodic slab geometry with a vacuum region of 21 Å in the out-of-plane direction (z direction) to avoid spurious interactions with periodic images. Both the atomic positions and in-plane lattice constants were optimized until the residual forces were below 0.001 eV/Å. To obtain phonon frequencies and vibration eigenvectors, the dynamic matrix was calculated using the finite difference scheme implemented in Phonopy.[50,51] Hellmann-Feynman forces in the $3 \times 3 \times 1$ supercell were computed by VASP for both positive and negative atomic displacements ($\delta = 0.03$ Å), and then used in Phonopy to construct the dynamic matrix. The diagonalization of the dynamic matrix provides phonon frequencies and eigenvectors. Raman intensity calculations were then performed within the Placzek approximation.[52] For the j-th phonon mode, the Raman intensity is $I \propto \frac{(n_j + 1)}{\omega_j}|e_i \cdot \tilde{R} \cdot e_s^T|^2$, where e_i and e_s are the electric polarization vectors of the incident and scattered lights, respectively, and $\tilde{R}$ is the Raman tensor of the phonon mode. The frequency of the j-th phonon mode and Boltzmann distribution function at a given temperature ($T = 300$ K in the present case) are given as ω_j and $n_j = (e^{\hbar\omega_j/k_B T} - 1)^{-1}$, respectively. The matrix element of the (3×3) Raman tensor, $\tilde{R}$, of the j-th phonon mode is then:[52,53]

$$\tilde{R}_{\alpha\beta}(j) = V_0 \sum_{\mu=1}^{N} \sum_{l=1}^{3} \frac{\partial \chi_{\alpha\beta}}{\partial r_l(\mu)} \frac{e_l^j(\mu)}{\sqrt{M_\mu}},$$

where $\chi_{\alpha\beta} = (\varepsilon_{\alpha\beta} - \delta_{\alpha\beta})/4\pi$ is the electric polarizability tensor related to the dielectric tensor $\varepsilon_{\alpha\beta}$, $r_l(\mu)$ is the position of the μ-th atom along the direction l, $\frac{\partial \chi_{\alpha\beta}}{\partial r_l(\mu)}$ is the derivative of the polarizability tensor (essentially the dielectric tensor) over the atomic displacement, $e_l^j(\mu)$ corresponds to the displacement of the μ-th atom along the direction l in the j-th phonon mode (i.e., the eigenvector of the dynamic matrix), M_μ is the mass of the μ-th atom, and V_0 is the unit cell volume. For both positive and negative atomic displacements ($\delta = 0.03$ Å) in the unit cell, the dielectric tensors $\varepsilon_{\alpha\beta}$ were computed by VASP at the experimental laser wavelength (532 nm in the present case) and thus their derivatives were obtained *via* the finite difference scheme. Based on the phonon frequencies, phonon eigenvectors, and the derivatives of dielectric tensors, the Raman tensor, $\tilde{R}$, of any phonon mode can be obtained. Averaging over all possible in-plane polarizations, the Raman intensity of any phonon mode in an experimental unpolarized laser configuration is given by $I \propto \frac{1}{4} \frac{(n_j + 1)}{\omega_j} |(|\tilde{R}_{11}|^2 + |\tilde{R}_{12}|^2 + |\tilde{R}_{21}|^2 + |\tilde{R}_{22}|^2)$. Finally, the Raman spectrum can be obtained after Lorentzian broadening based on the calculated Raman intensities, $I(j)$, and phonon frequencies, ω_j.

Acknowledgements

Author Contributions

Y.-C.L. performed the PLD experiments. Y.-C.L., A.A.P., D.B.G., and A.S. performed the *in situ* diagnostics. C.L., G.D., and M.F.C. performed the STEM measurements. G.D., Y.-C.L., and C.L. carried out post-imaging analysis on the experimental HAADF images. Y.Y. and Y.G. grew the WS_2 monolayer crystals. E.Z. performed the MD simulations. M.Y. performed the DFT structure calculations. L.L. and X.K. calculated the predicted Raman spectra. H.M.M. performed the XPS measurements. M.L. performed the MALDI measurements. Y.-C.L., A.P., I.I., C.M.R. performed or assisted in the PL and Raman measurements. Y.-C.L., D.B.G., K.X., and A.A.P. conceived the experiments and co-wrote the paper. We thank S.T. King for his assistance on the MALDI experiments. The authors declare no competing financial interests.

Supporting Information Available

Notes concerning selenization of 1L MoS_2 to form Janus MoSSe and related characterization, and theoretical methods to calculate the Raman spectra of Janus WSSe and MoSSe monolayers. Table of calculated frequencies of phonon modes of pristine TMDs and Janus MLs; Example ion probe waveforms for Se plasma propagation; MALDI mass spectrum of Se clusters; Optical emission spectra of Se plumes; Laser induced fluorescence of propagating selenium species; Photoluminescence from selenized $WS_{2-x}Se_x$ crystals at different pressures and temperatures; DFT calculation of Se adatom diffusion through WS_2; MD simulation snapshots (and movies) of Se_2 cluster impacts with WS_2 ML with increasing kinetic energies; MD simulation snapshots (and movies) of Se_9 cluster impacts with WS_2 ML with increasing kinetic energies; MD simulation snapshots (and movies) of the structural reorganization processes occurring following implantation of Se_9 into WS_2; HAADF Z-STEM images of Se-irradiated WS_2 at 200 °C; Summary for Raman and PL spectra of Janus WSSe and MoSSe ML; Schematic illustrations of the atomic displacements of the optical phonon modes in WS_2 and Janus WSSe ML; Calculated phonon dispersion of WSSe ML, Optical and SEM images of converted Janus WSSe ML; First-principles modeling of $WS_{2(1-x)}Se_{2x}$ structures with different structures and Se content x. This material is available free of charge *via* the Internet at http://pubs.acs.org.

References

1. Chhowalla, M.; Shin, H. S.; Eda, G.; Li, L.-J.; Loh, K. P.; Zhang, H. The Chemistry of Two-Dimensional Layered Transition Metal Dichalcogenide Nanosheets. *Nat. Chem.* **2013**, *5*, 263–275.

2. Manzeli, S.; Ovchinnikov, D.; Pasquier, D.; Yazyev, O. V.; Kis, A. 2D Transition Metal Dichalcogenides. *Nat. Rev. Mater.* **2017**, *2*, 17033.

3. Komsa, H.-P.; Krasheninnikov, A. V. Two-Dimensional Transition Metal Dichalcogenide Alloys: Stability and Electronic Properties. *J. Phys. Chem. Lett.* **2012**, *3*, 3652–3656.

4. Mahjouri-Samani, M.; Lin, M.-W.; Wang, K.; Lupini, A. R.; Lee, J.; Basile, L.; Boulesbaa, A.; Rouleau, C. M.; Puretzky, A. A.; Ivanov, I. N.; Xiao, K.; Yoon, M.; Geohegan, D. B.; Patterned Arrays of Lateral Heterojunctions within Monolayer Two-Dimensional Semiconductors. *Nat. Commun.* **2015**, *6*, 7749.

5. Duan, X.; Wang, C.; Fan, Z.; Hao, G.; Kou, L.; Halim, U.; Li, H.; Wu, X.; Wang, Y.; Jiang, J.; Pan, A.; Huang, Y.; Yu, R.; Duan, X.; Synthesis of $WS_{2x}Se_{2-2x}$ Alloy Nanosheets with Composition-Tunable Electronic Properties. *Nano Lett.* **2016**, *16*, 264–269.

6. Li, X.; Puretzky, A. A.; Sang, X.; KC, S.; Tian, M.; Ceballos, F.; Mahjouri-Samani, M.; Wang, K.; Unocic, R. R.; Zhao, H.; Duscher, G.; Cooper, V. R.; Rouleau, C. M.; Geohegan, D. B.; Xiao, K.; Suppression of Defects and Deep Levels Using Isoelectronic Tungsten Substitution in Monolayer $MoSe_2$. *Adv. Funct. Mater.* **2017**, *27*, 1603850.

7. Yu, P.; Lin, J.; Sun, L.; Le, Q. L.; Yu, X.; Gao, G.; Hsu, C.-H.; Wu, D.; Chang, T.-R.; Zeng, Q.; Liu, F.; Wang, Q. J.; Jeng, H.-T.; Lin, H.; Trampert, A.; Shen, Z.; Suenaga, K.; Liu, Z.; Metal-Semiconductor Phase-Transition in $WSe_{2(1-x)}Te_{2x}$ Monolayer. *Adv. Mater.* **2017**, *29*, 1603991.

8. Susarla, S.; Kutana, A.; Hachtel, J. A.; Kochat, V.; Apte, A.; Vajtai, R.; Idrobo, J. C.; Yakobson, B. I.; Tiwary, C. S.; Ajayan, P. M. Quaternary 2D Transition Metal Dichalcogenides (TMDs) with Tunable Bandgap. *Adv. Mater.* **2017**, *29*, 1702457.

9. Li, H.; Liu, H.; Zhou, L.; Wu, X.; Pan, Y.; Ji, W.; Zheng, B.; Zhang, Q.; Zhuang, X.; Zhu, X.; Wang, X.; Duan, X.; Pan, A.; Strain-Tuning Atomic Substitution in Two-Dimensional Atomic Crystals. *ACS Nano* **2018**, *12* 4853–4860.

10. Kang, J.; Tongay, S.; Li, J.; Wu, J. Monolayer Semiconducting Transition Metal Dichalcogenide Alloys: Stability and Band Bowing. *J. Appl. Phys.* **2013**, *113*, 143703.

11. Riis-Jensen, A. C.; Deilmann, T.; Olsen, T.; Thygesen, K. S. Classifying the Electronic and Optical Properties of Janus Monolayers. *ACS Nano* **2019**, *13*, 13354–13364.

12. Lu, A.-Y.; Zhu, H.; Xiao, J.; Chuu, C.-P.; Han, Y.; Chiu, M.-H.; Cheng, C.-C.; Yang, C.-W.; Wei, K.-H.; Yang, Y.; Wang, Y.; Sokaras, D.; Nordlund, D.; Yang, P.; Muller, D. A.; Chou, M.-Y.; Zhang, X.; Li, L.-J.; Janus Monolayers of Transition Metal Dichalcogenides. *Nat. Nanotechnol.* **2017**, *12*, 744–749

13. Zhang, J.; Jia, S.; Kholmanov, I.; Dong, L.; Er, D.; Chen, W.; Guo, H.; Jin, Z.; Shenoy, V. B.; Shi, L.; Lou, J.; Janus Monolayer Transition-Metal Dichalcogenides. *ACS Nano* **2017**, *11*, 8192–8198.

14. Dong, L.; Lou, J.; Shenoy, V. B. Large In-Plane and Vertical Piezoelectricity in Janus Transition Metal Dichalchogenides. *ACS Nano* **2017**, *11*, 8242–8248.

15. Kang, J.; Tongay, S.; Zhou, J.; Li, J.; Wu, J. Band Offsets and Heterostructures of Two-Dimensional Semiconductors. *Appl. Phys. Lett.* **2013**, *102*, 012111.

16. Komsa, H.-P.; Kotakoski, J.; Kurasch, S.; Lehtinen, O.; Kaiser, U.; Krasheninnikov, A. V. Two-Dimensional Transition Metal Dichalcogenides under Electron Irradiation: Defect Production and Doping. *Phys. Rev. Lett.* **2012**, *109*, 035503.

17. Ghorbani-Asl, M.; Kretschmer, S.; Spearot, D. E.; Krasheninnikov, A. V. Two-Dimensional MoS$_2$ under Ion Irradiation: From Controlled Defect Production to Electronic Structure Engineering. *2D Mater.* **2017**, *4*, 025078.

18. Ma, Q.; Isarraraz, M.; Wang, C. S.; Preciado, E.; Klee, V.; Bobek, S.; Yamaguchi, K.; Li, E.; Odenthal, P. M.; Nguyen, A.; Barroso, D.; Sun, D.; von Son Palacio, G.; Gomez, M.; Nguyen, A.; Le, D.; Pawin, G.; Mann, J.; Heinz, T. F.; Rahman, T. S.; *et al.* Postgrowth Tuning of the Bandgap of Single-Layer Molybdenum Disulfide Films by Sulfur/Selenium Exchange. *ACS Nano* **2014**, *8*, 4672–4677.

19. Cheng, Z.; Abuzaid, H.; Yu, Y.; Zhang, F.; Li, Y.; Noyce, S. G.; Williams, N. X.; Lin, Y.-C.; Doherty, J. L.; Tao, C.; Cao, L.; Franklin, A. D.; Convergent Ion Beam Alteration of 2D Materials and Metal-2D Interfaces. *2D Mater.* **2019**, *6*, 034005.

20. Huang, B.; Tian, F.; Shen, Y.; Zheng, M.; Zhao, Y.; Wu, J.; Liu, Y.; Pennycook, S. J.; Thong, J. T. L. Selective Engineering of Chalcogen Defects in MoS$_2$ by Low-Energy Helium Plasma. *ACS Appl. Mater. Interfaces* **2019**, *11*, 24404–24411.

21. Bangert, U.; Pierce, W.; Kepaptsoglou, D. M.; Ramasse, Q.; Zan, R.; Gass, M. H.; Van den Berg, J. A.; Boothroyd, C. B.; Amani, J.; Hofsäss, H. Ion Implantation of Graphene—Toward IC Compatible Technologies. *Nano Lett.* **2013**, *13*, 4902–4907.

22. Bangert, U.; Stewart, A.; O'Connell, E.; Courtney, E.; Ramasse, Q.; Kepaptsoglou, D.; Hofsäss, H.; Amani, J.; Tu, J. S.; Kardynal, B. Ion-Beam Modification of 2-D Materials - Single Implant Atom Analysis *via* Annular Dark-Field Electron Microscopy. *Ultramicroscopy* **2017**, *176*, 31–36.

23 Lowndes, D. H.; Geohegan, D. B.; Puretzky, A. A.; Norton, D. P.; Rouleau, C. M. Synthesis of Novel Thin-Film Materials by Pulsed Laser Deposition. *Science* **1996**, *273*, 898–903.

24 Mahjouri-Samani, M.; Gresback, R.; Tian, M.; Wang, K.; Puretzky, A. A.; Rouleau, C. M.; Eres, G.; Ivanov, I. N.; Xiao, K.; McGuire, M. A.; Duscher, G.; Geohegan, D. B.; Pulsed Laser Deposition of Photoresponsive Two-Dimensional GaSe Nanosheet Networks. *Adv. Funct. Mater.* **2014**, *24*, 6365–6371.

25. Mahjouri-Samani, M.; Tian, M.; Puretzky, A. A.; Chi, M.; Wang, K.; Duscher, G.; Rouleau, C. M.; Eres, G.; Yoon, M.; Lasseter, J.; Xiao, K.; Geohegan, D. B.; Nonequilibrium Synthesis of TiO$_2$ Nanoparticle "Building Blocks" for Crystal Growth by Sequential Attachment in Pulsed Laser Deposition. *Nano Lett.* **2017**, *17*, 4624–4633.

26. Puretzky, A. A.; Geohegan, D. B.; Hurst, G. B.; Buchanan, M. V.; Luky'anchuk, B. S. Imaging of Vapor Plumes Produced by Matrix Assisted Laser Desorption: A Plume Sharpening Effect. *Phys. Rev. Lett.* **1999**, *83*, 444–447.

27. Geohegan, D. B.; Puretzky, A. A.; Rouleau, C.; Jackson, J.; Eres, G.; Liu, Z.; Styers-Barnett, D.; Hu, H.; Zhao, B.; Ivanov, I.; Xiao, K.; More, K.; Laser Interactions in Nanomaterials Synthesis. In *Laser-Surface Interactions for New Materials Production*; Miotello, A., Ossi, P. M., Eds; Springer Verlag: Berlin-Heidelberg, 2010; pp 1–15.

28. Knox, B. E. Mass Spectrometric Studies of Laser-Induced Vaporization. I. Selenium. *Mater. Res. Bull.* **1968**, *3*, 329–336.

29. Hearley, A. K.; Johnson, B. F. G.; McIndoe, J. S.; Tuck, D. G. Mass Spectrometric Identification of Singly-Charged Anionic and Cationic Sulfur, Selenium, Tellurium and Phosphorus Species Produced by Laser Ablation. *Inorganica Chim. Acta* **2002**, *334*, 105–112.

30. Kooser, K.; Ha, D. T.; Itälä, E.; Laksman, J.; Urpelainen, S.; Kukk, E. Size Selective Spectroscopy of Se Microclusters. *J. Chem. Phys.* **2012**, *137*, 044304.

31. Pan, B. C.; Han, J. G.; Yang, J.; Yang, S. Theoretical Studies of Neutral and Cationic Selenium Clusters. *Phys. Rev. B* **2000**, *62*, 17026–17030.

32. Fedrigo, S.; Harbich, W.; Buttet, J. Soft Landing and Fragmentation of Small Clusters Deposited in Noble-Gas Films. *Phys. Rev. B* **1998**, *58*, 7428–7433.

33. Barrow, R. F.; Chandler, G. G.; Meyer, C. B. The B $(3\sum u-)$-X$(3\sum g-)$ Band System of the SeFormula Molecule. *Philos. Trans. R. Soc. A Math. Phys. Eng. Sci.* **1966**, *260*, 395–452.

34. Berkdemir, A.; Gutiérrez, H. R.; Botello-Méndez, A. R.; Perea-López, N.; Elías, A. L.; Chia, C.-I.; Wang, B.; Crespi, V. H.; López-Urías, F.; Charlier, J.-C.; Terrones, H.: M. Terrones; Identification of Individual and Few Layers of WS_2 Using Raman Spectroscopy. *Sci. Rep.* **2013**, *3*, 1755.

35. Kandemir, A.; Sahin, H. Bilayers of Janus WSSe: Monitoring the Stacking Type *via* the Vibrational Spectrum. *Phys. Chem. Chem. Phys.* **2018**, *20*, 17380–17386.

36. Popok, V. N.; Barke, I.; Campbell, E. E. B.; Meiwes-Broer, K.-H. Cluster–Surface Interaction: From Soft Landing to Implantation. *Surf. Sci. Rep.* **2011**, *66*, 347–377.

37. Palsgaard, M.; Gunst, T.; Markussen, T.; Thygesen, K. S.; Brandbyge, M. Stacked Janus Device Concepts: Abrupt pn-Junctions and Cross-Plane Channels. *Nano Lett.* **2018**, *18*, 7275–7281.

38. Haberland, H.; Insepov, Z.; Moseler, M. Molecular-Dynamics Simulation of Thin-Film Growth by Energetic Cluster Impact. *Phys. Rev. B* **1995**, *51*, 11061–11067.

39. Jackson, J. J.; Puretzky, A. A.; More, K. L.; Rouleau, C. M.; Eres, G.; Geohegan, D. B. Pulsed Growth of Vertically Aligned Nanotube Arrays with Variable Density. *ACS Nano* **2010**, *4*, 7573–7581.

40. Koch, C. Determination of Core Structure Periodicity and Point Defect Density along Dislocations. PhD Thesis, Arizona State University, Tempe, AZ, **2002**

41. Vercauteren, T.; Pennec, X.; Perchant, A.; Ayache, N.; Antipolis, I. S.; Antipolis, S. Diffeomorphic Demons Using ITK's Finite Difference Solver Hierarchy. *Insight J.* **2007**, *154*, 1–8.

42. Plimpton, S. Fast Parallel Algorithms for Short-Range Molecular Dynamics. *J. Comput. Phys.* **1995**, *117*, 1–19.

43. Mobaraki, A.; Kandemir, A.; Yapicioglu, H.; Gülseren, O.; Sevik, C. Validation of Inter-Atomic Potential for WS_2 and WSe_2 Crystals through Assessment of Thermal Transport Properties. *Comput. Mater. Sci.* **2018**, *144*, 92–98.

44. Ziegler, J. F.; Biersack, J. P.; Littmark, U. *The Stopping and Range of Ions in Matter*; Pergamon: New York, 1985.

45. Stukowski, A. Visualization and Analysis of Atomistic Simulation Data with OVITO-The Open Visualization Tool. *Model. Simul. Mater. Sci. Eng.* **2010**, *18*.

46. Kresse, G.; Furthmüller, J. Efficient Iterative Schemes for *Ab Initio* Total-Energy Calculations Using a Plane-Wave Basis Set. *Phys. Rev. B* **1996**, *54*, 11169–11186.

47. Perdew, J. P.; Zunger, A. Self-Interaction Correction to Density-Functional Approximations for Many-Electron Systems. *Phys. Rev. B* **1981**, *23*, 5048–5079.

48. Molina-Sánchez, A.; Wirtz, L. Phonons in Single-Layer and Few-Layer MoS_2 and WS_2. *Phys. Rev. B - Condens. Matter Mater. Phys.* **2011**, *84*, 155413.

49. Zhao, Y.; Luo, X.; Li, H.; Zhang, J.; Araujo, P. T.; Gan, C. K.; Wu, J.; Zhang, H.; Quek, S. Y.; Dresselhaus, M. S.; Xiong, Q.; Interlayer Breathing and Shear Modes in Few-Trilayer MoS_2 and WSe_2. *Nano Lett.* **2013**, *13*, 1007–1015.

50. Togo, A.; Oba, F.; Tanaka, I. First-Principles Calculations of the Ferroelastic Transition between Rutile-Type and $CaCl_2$-Type SiO_2 at High Pressures. *Phys. Rev. B - Condens. Matter Mater. Phys.* **2008**, *78*, 134106.

51. Liang, L.; Meunier, V. Electronic and Thermoelectric Properties of Assembled Graphene Nanoribbons with Elastic Strain and Structural Dislocation. *Appl. Phys. Lett.* **2013**, *102*, 143101.

52. Liang, L.; Meunier, V. First-Principles Raman Spectra of MoS_2, WS_2 and Their Heterostructures. *Nanoscale* **2014**, *6*, 5394–5401.

53. Umari, P.; Pasquarello, A.; Dal Corso, A. Raman Scattering Intensities in α-Quartz: A First-Principles Investigation. *Phys. Rev. B - Condens. Matter Mater. Phys.* **2001**, *63*, 094305.